https://doi.org/10.1016/j.corsci.2017.02.001

High-temperature oxidation behavior of laser-aided additively manufactured NiCrAlY coating

M. Ansari[a] R. Shoja-Razavi[b] M. Barekat[b] H.C.Man[c]

a

a. Young Researchers and Elite Club, Najafabad Branch, Islamic Azad University, Najafabad, Iran

b

b. Department of Materials Engineering, Malek Ashtar University of Technology, Shahin Shahr, Isfahan, Iran

c

c. Department of Industrial and Systems Engineering, The Hong Kong Polytechnic University, Hong Kong, China

Abstract

In this study, NiCrAlY coatings were additively manufactured on the surface of IN738 substrate through a laser-aided additive manufacturing approach. The high-temperature oxidation behavior of freestanding coatings at 1200 °C was also investigated. The coatings were thick, dense, and well-bonded with dendritic γ/β microstructure. The results proved that the coatings were able to withstand the operating temperature of 1200 °C for up to ten cycles. After ten cycles of oxidation, the oxide scales formed on the coatings were mainly composed of α-Al_2O_3 and $Al_5Y_3O_{12}$ phases; however, NiO, Cr_2O_3 and $Ni(Cr,Al)_2O_4$ phases were not detected.

Keywords: A. Superalloys; B. Metal coatings; C. High-temperature corrosion D. Oxidation

1. Introduction

Additive manufacturing (AM) processes, regardless of the heat source and raw material supplement, have had substantial growth and have captured the attention of various industries in numerous application-oriented sectors [1], [2]. With the rapid increase of interest in additive manufacturing of bulk materials, the application of AM-based processes for preparing coatings is likely to become more popular. Recent advances in high-accuracy integrated motion systems together with the possibilities of consolidating advanced materials into desired shapes on the substrate have made inroads into the concept of surface engineering through AM-based processes [3]. This novel approach can be successfully employed for repair and surface protection applications, particularly for complex geometries and strategic materials, which offers some advantages such as precision, flexibility, efficiency, and economy novelty of processing [4], [5]. Among AM-based processes, laser-aided additive manufacturing (LAM) process based on either directed energy deposition or powder bed fusion can be effectively employed for the purposes of surface engineering so as to manufacture dense protective coatings [6], [7]. Nickel-based superalloys, particularly IN738LC, have been widely used for hot-section components of gas turbines. These hot-section components are exposed to an extremely oxidative and corrosive environment at high operating temperatures and consequently the high-temperature degradation can decrease the lifespan and efficiency of the components. In view of this, MCrAlY overlay coatings (where the M stands for Fe, Ni, Co or Ni + Co

combination) can be effectively employed in order to protect hot-section components of gas turbines. The excellent oxidation resistance of MCrAlY overlay coatings is attributed to the formation of adherent alumina scales with slow grow rate as a result of the reactive element yttrium effects [8].
The high Cr and Al contents of the MCrAlY overlay coatings can ensure good protection against corrosion and oxidation. However, the lifespan of MCrAlY overlay coatings during thermal oxidation is assessed in relation to the consumption level of the aluminum reservoir to grow the oxide scale. When severe aluminum depletion happens, the oxide scale cannot protect the substrate and some detrimental oxides like NiO and $Ni(Cr,Al)_2O_4$ spinel can form and cause cracking and eventually spallation of the oxide scale [9], [10]. Therefore, the availability of aluminum is an essential determinant of oxidation life. Moreover, the contribution of yttrium as a reactive element to the alumina scale adhesion, growth, and microstructure must be considered as an important factor on the oxidation behavior [11].

It has been found in previous studies [12], [13], [14], [15], [16], [17], [18] that not only does the oxidation resistance of MCrAlY overlay coatings depend on the chemical composition but also it depends on the microstructure. In addition, the initial quality of MCrAlY overlay coatings has an indispensable influence on the contribution of reactive element yttrium [11]. All these circumstances rely on manufacturing processes and processing parameters that can affect the oxidation behavior. MCrAlY overlay coatings are frequently manufactured by means of thermal spraying processes in practice [19], [20], but these processes produce polycrystalline layers with random crystal orientation, low-to-medium porosity, and weak mechanical bonding. The random crystal orientation of thermally sprayed MCrAlY coatings results in reduced thermo-mechanical fatigue strength of the coating [21]. In addition,

the porosities allow the oxygen to diffuse through the coatings and consequently decrease the high-temperature oxidation resistance. Surface engineering through LAM process can be a good alternative to thermal spraying processes that can simultaneously ensure high-temperature oxidation, creep and thermal fatigue resistance of MCrAlY coatings by producing homogeneous and dense coatings with preferred crystal orientation and strong metallurgical bonding [21], [22]. Although there are several studies in the literature on the high-temperature oxidation behavior of laser-aided additively manufactured MCrAlY coatings mostly at 1000 and 1100 °C [23], [24], [25], [26], [27], [28], to date there is no study on the oxidation behavior of laser-aided additively manufactured MCrAlY coatings at 1200 °C. Considering the fact that thermally sprayed MCrAlY coatings have shown poor oxidation resistance at temperatures above 1100 °C because of the rapid failure of the protective α-Al_2O_3 scale [29], [30], [31] and that laser-aided additively manufactured MCrAlY coatings have more advantages compared to thermally sprayed MCrAlY coatings, thus it can be expected that MCrAlY coatings manufactured through LAM process can withstand operating temperatures above 1100 °C. In regard to this, the present research aims to address the lack of basic knowledge that exists of the oxidation behavior of laser-aided additively manufactured NiCrAlY coatings at temperatures above 1100 °C. Furthermore, this research presents a study on microstructure, phase formation, and high-temperature oxidation behavior of NiCrAlY coatings manufactured through LAM process.

2. Material and methods

In this study, IN738LC superalloy coupons of size 100 × 100 × 5 mm, used as the substrate, were cut from casted part with no heat treatment using wire electrical discharge machining (WEDM). Gas atomized Ni 20Cr 10Al 1Y

powder (PAC9620AM) was used as an additive material with a grain size distribution of −100 + 50 μm (−140 + 270 mesh). The chemical composition of both substrate and additive material is given in Table 1.

Table 1. Chemical composition of the additive powder and substrate.

Material	Form	Element (wt.%)											
Empty Cell	Empty Cell	Ni	Cr	Al	Y	Co	W	Ti	Ta	Mo	Nb	C	Other
NiCrAlY	Powder	Bal.	21.02	9.92	0.95	–	–	–	–	–	–	–	<0.20
IN738LC	Plate	Bal.	13.6	2.9	–	9.1	4.9	4.4	3.1	1.7	0.1	0.1	<0.11

The setup for directed energy deposition-based LAM process is as follows: a pulsed Nd:YAG laser with a maximum power of 700 W integrated with an XYZ-Rotation CNC machine; a powder feeder for blowing the additive powder in combination with a four-way coaxial nozzle for focusing the powder stream into the laser beam. The optimum single-layer LAM conditions are as follows: laser power of 300 W, scanning speed of 4 mm/s and powder feeding rate of 250 mg/s. Other laser parameters such as defocused beam spot diameter, frequency, and pulse duration were fixed at 1 mm, 35 Hz, and 3 ms, respectively. Argon (20 L/min) was used as a powder carrier and shielding gas. Full details of the process optimization of single-layer LAM conditions are described elsewhere [32]. The final layer for oxidation tests was achieved using the optimum single-layer LAM conditions and side by side overlapping single tracks with 65% overlapping ratio.

After LAM process, the additively manufactured portion was removed from the substrate by wire electrical discharge machining (WEDM). The oxidation test

pieces with the dimensions $10_w \times 10_l \times 0.4_t$ mm were cut from the center of the additively manufactured portion, were ground using 500 grit SiC emery paper, and ultrasonically cleaned in acetone. Discontinuous oxidation tests were performed in a tube furnace in static air. Each test piece was inserted into an individual alumina crucible and then put into the furnace at room temperature for applying the subsequent thermal cycle. As schematically shown in Fig. 1, the thermal cycle involved heating to the temperature of 1200 °C with the constant rate of 10 °C/min, maintaining for 10 h, and then furnace cooling. The test pieces were inside of the furnace during heating and cooling process. After completion of each cycle, the crucibles were removed out of the furnace and weighed using an analytical balance (TE214S, Sartorius) with an accuracy of 0.1 mg. The total weight of the crucibles and test pieces was recorded. The oxidation behavior was assessed by five individual measurements for the gross weight gains (test piece + spalled oxide) of five test pieces. Overall, ten cycles were applied for evaluation of oxidation behavior.

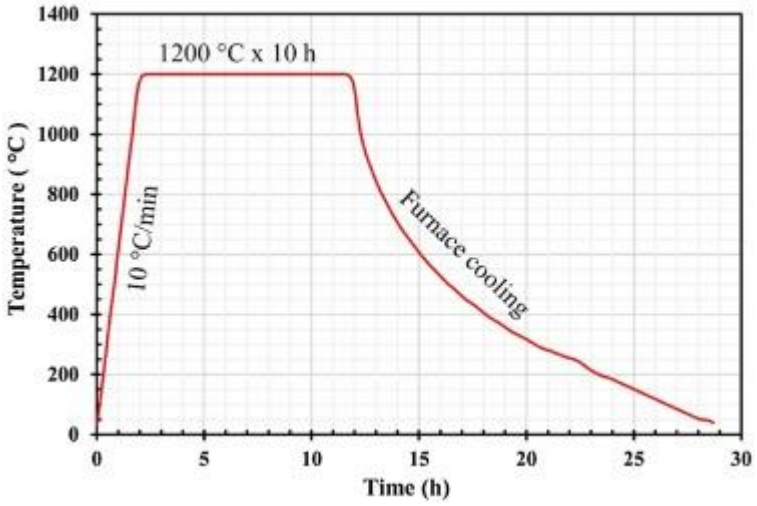

Fig 1. Schematic thermal history of a single cycle of oxidation used in this study.

Before oxidation tests, the cross-section of all coated specimens was ground and polished using standard metallographic techniques and then etched with

Kalling's No. 2 reagent for microstructural observations. The microstructural evaluation, as well as the chemical composition of the coatings before and after oxidation tests, were examined by FE-SEM (MIRA3, TESCAN) electron imaging equipped with an energy dispersive X-ray spectrometry (EDS) analyzer. Phase identification of the coatings before and after oxidation tests was carried out by X-ray diffraction (XRD) (X'Pert Pro, Phillips) with Cu Ka radiation at 40 kV, 40 mA, and scanned within 2θ = 20–90°.

3. Results

3.1. Microstructure

Fig. 2 shows SEM micrograph of a transverse cross-section of the laser-aided additively manufactured NiCrAlY coating achieved at laser power of 300 W, scanning speed of 4 mm/s, powder feeding rate of 250 mg/s, and 65% side by side overlapping ratio. A thick, dense, and well-bonded NiCrAlY coating was achieved through LAM process. The thickness of the coating was about 600 μm. Fig. 3 shows high magnification SEM micrograph of Fig. 2, which can represent the microstructure in detail. Fig. 3 shows an oriented γ/β structure in the lower part of the coating. In the lower part, oriented columnar γ dendrites grew almost perpendicularly to the substrate. A transition from the oriented γ/β structure to an un-oriented γ/β structure noticed in the middle of the coating. Large amounts of randomly oriented γ dendrites can be observed in the upper part of the coating.

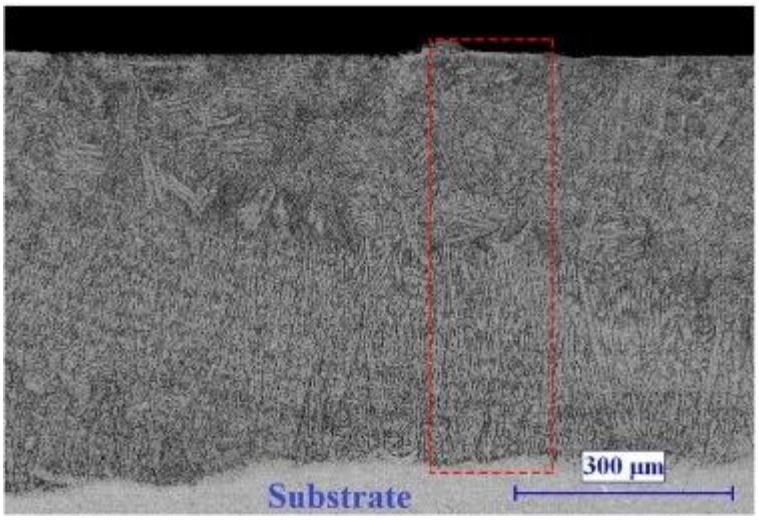

Fig. 2. Cross-sectional microstructure of NiCrAlY coating manufactured through LAM process on IN738LC achieved at laser power of 300 W, scanning speed of 4 mm/s, powder feeding rate of 250 mg/s, and 65% side by side overlapping ratio.

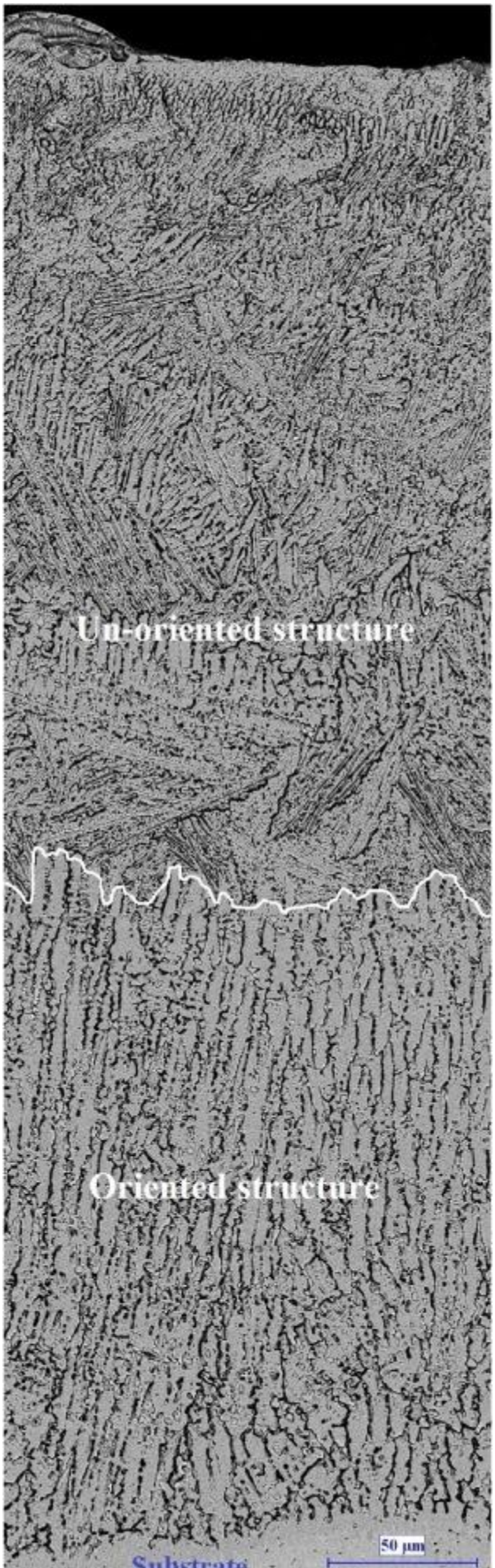
Un-oriented structure
Oriented structure
50 μm
Substrate

Fig. 3. High-magnification microstructure observation of the selected region shown in Fig. 2.

The formation of the above-mentioned phases was also confirmed by XRD results. The phases were identified as γ and β in the coating, whereas γ´-Ni_3Al was not detected. Interestingly, it is reported that high aluminum content of γ/β MCrAlY coatings improves the corrosion and oxidation resistance compared to γ/γ´ MCrAlY coatings [33]. The high aluminum content of the NiCrAlY coating used in this study can allow the growth of a compact alumina scale and consequently a good oxidation resistant is expected.

3.2. High-temperature oxidation

3.2.1. Weight gain

The gross weight gains (test piece + spalled oxide) as a function of the number of cycles for five individual samples are shown in Fig. 4. The oxidation behavior is almost the same for five samples. The gross weight increased with time and the oxidation behavior looks quite close to a parabolic or sub-parabolic rate law, which is common for alumina formers. After first two cycles, the coatings showed a sharp initial weight gain at the beginning of the oxidation. At longer oxidation duration, the coatings showed a trend of slow weight gain and the rate of oxidation became almost constant. It means that the oxygen diffusion into the coatings become negligible, which shows that the coatings resist up to ten cycles at 1200 °C.

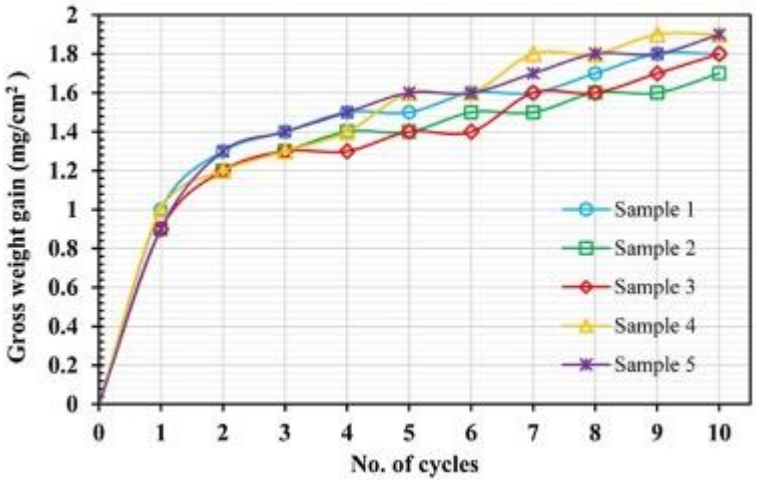

Fig. 4. Gross weight gain (test piece + spalled oxide) for five samples during ten cycles of oxidation at 1200 °C.

3.2.2. Characteristics of oxide scale

Fig. 5 shows the XRD patterns of the NiCrAlY coatings before and after oxidation tests for two and ten cycles of oxidation at 1200 °C. The predominant phases in the coating before oxidation tests were γ-Ni and β-NiAl, but γ´-Ni_3Al was not detected (Fig. 5a). The oxide products on the oxidized coatings were composed of α-Al_2O_3 (space group: R-3c, rhombohedral) and $Al_5Y_3O_{12}$ (space group: Ia3d, cubic), but NiO, Cr_2O_3 and $Ni(Al/Cr)_2O_4$ phases were not detected (Fig. 5b and c). The relative intensity of α-Al_2O_3 increased with increasing the number of cycles, which implies the thickening of the oxide scale with time; however, the relative intensity of $Al_5Y_3O_{12}$ decreased. The γ-Ni and β-NiAl phases from the coating were still present after oxidation tests, but the relative intensity of γ-Ni phase increased, while the relative intensity of β-NiAl phase decreased.

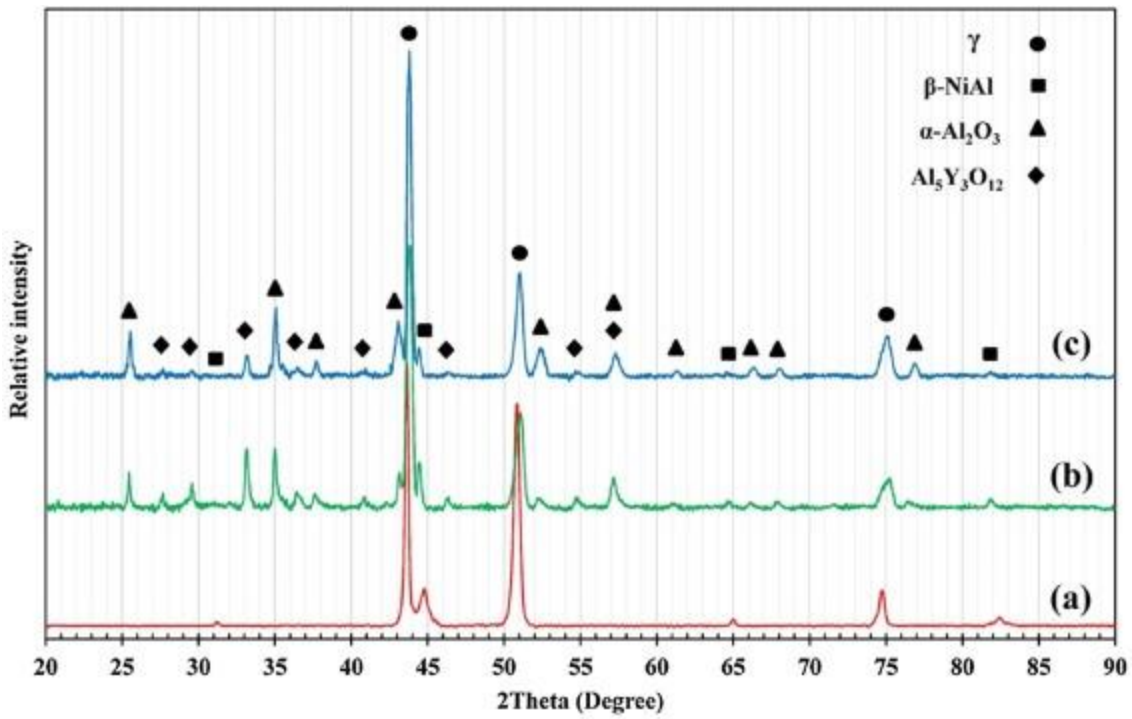

Fig. 5. XRD patterns of the coating, (a) before oxidation tests, (b) after two cycles, and (c) after ten cycles of oxidation at 1200 °C.

Fig. 6, Fig. 7 show the cross-sectional SEM micrographs of the oxide scales on the NiCrAlY coatings after two and ten cycles as well as their corresponding EDS elemental maps. After two cycles (Fig. 6), the oxide scale only consisted of α-Al_2O_3 and $Al_5Y_3O_{12}$ islands and pegs while Cr and Ni elements did not exist in the oxide scale and they were present just below the scale/coating interface. Moreover, it seems that the coating is over-doped by reactive element Y, which resulted in an extensive precipitation of $Al_5Y_3O_{12}$ protrusions (pegs) at the scale/coating interface. $Al_5Y_3O_{12}$ phase was also present at the surface of alumina scale to form a thin non-protective porous oxide. The average thickness of oxide scale was about 5 μm.

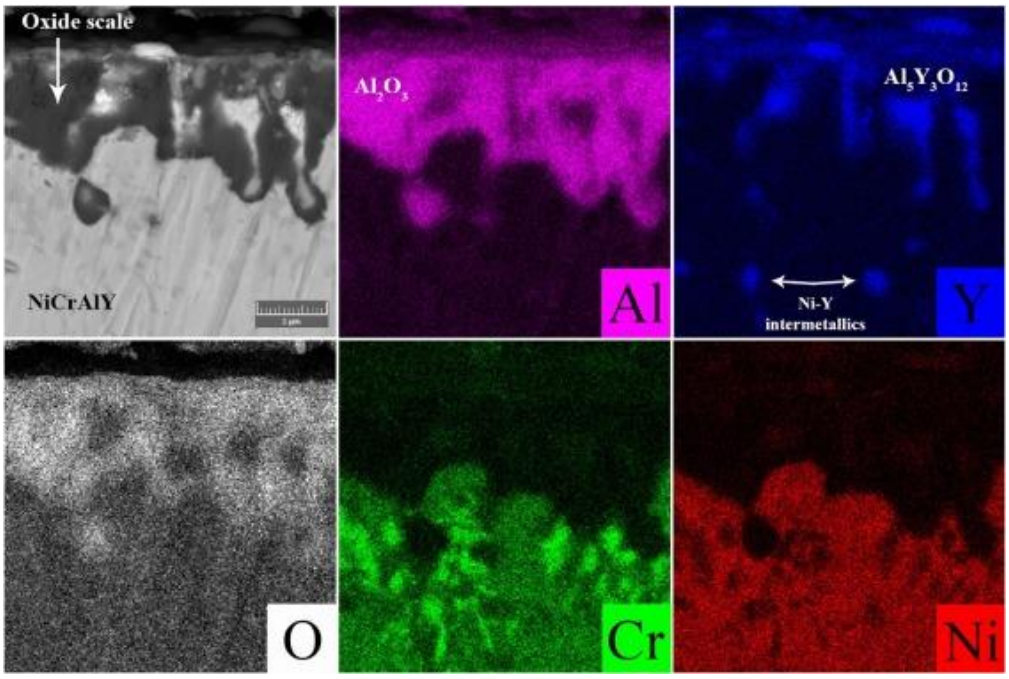

Fig. 6. Cross-sectional SEM micrograph and corresponding EDS elemental maps of the oxide scale after two cycles of oxidation at 1200 °C.

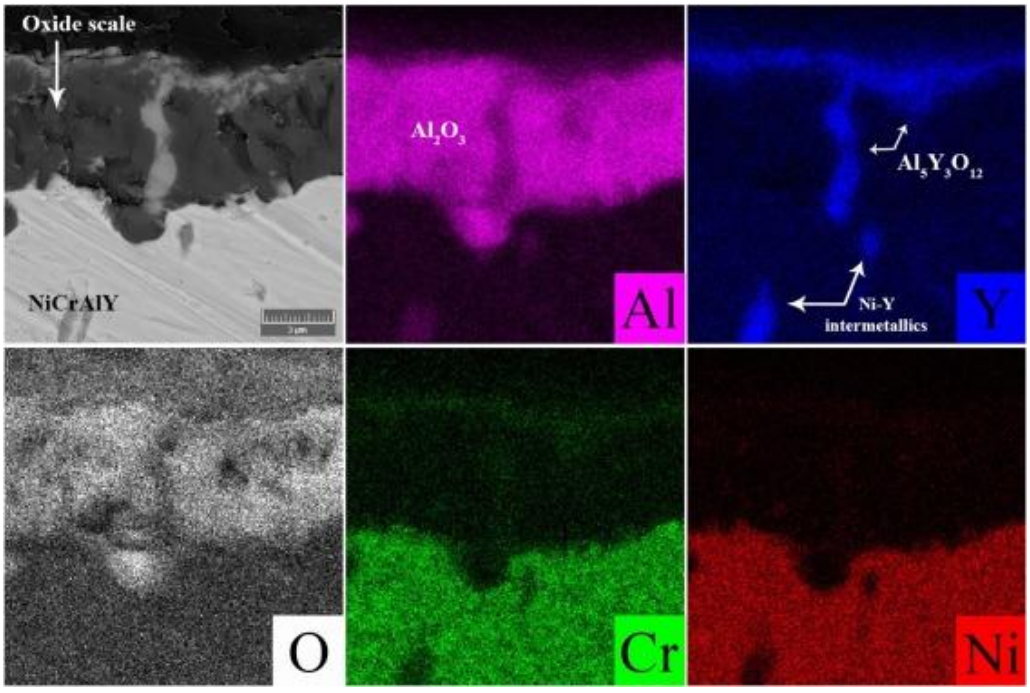

Fig. 7. Cross-sectional SEM micrograph and corresponding EDS elemental maps of the oxide scale after ten cycles of oxidation at 1200 °C.

After ten cycles (Fig. 7), the oxide scale contained α-Al_2O_3 scale with few protrusions at the scale/coating interface. $Al_5Y_3O_{12}$ particles were rarely present in the α-Al_2O_3 scale and the $Al_5Y_3O_{12}$ phase was present at the surface of alumina scale as a thin non-protective porous oxide. This outer thin oxide underwent spallation. The average thickness of oxide scale was about 8 μm. Cr and Ni elements did not exist in the oxide scale and they were only present below the scale/coating interface. No internal oxidation was observed in the underlying NiCrAlY coatings.

3.2.3. Analysis of oxidized surfaces

Low-magnification SEM micrographs showing the surface morphology of the oxidized coatings after two and ten cycles at 1200 °C are shown in Fig. 8, Fig. 10, respectively. The top surface of the oxidized NiCrAlY coating after two cycles (Fig. 8) seemed to be overlaid with a fairly dense gray scale. However, some inclusions, similar to cracks, were visible as darker and brighter objects (Fig. 9). The results of EDS analysis for different zones in Fig. 9 are summarized in Table 2, which indicates that the black phase (Zone A) is α-Al_2O_3 oxide, the gray phase (Zone B) is $Al_5Y_3O_{12}$ oxide, and the white phase (Zone C) is bare coating. In fact, the bare coating was visible because of cracks and it was being re-oxidized to fill the cracks. Furthermore, there was a slight spallation of $Al_5Y_3O_{12}$ oxide after two cycles.

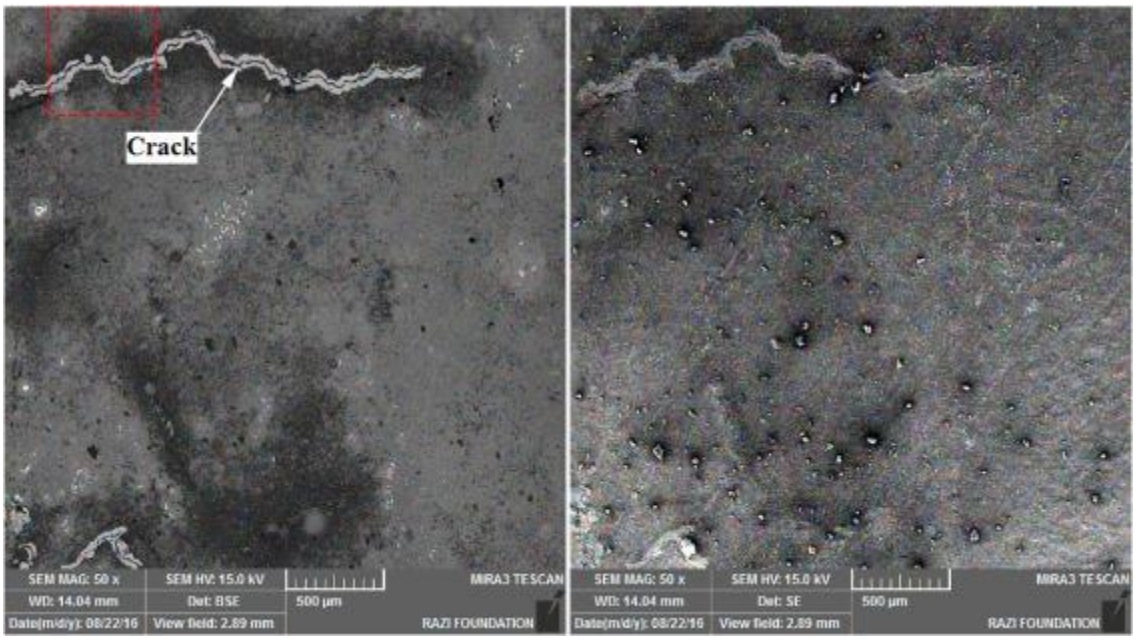

Fig. 8. Low-magnification backscatter and secondary electron SEM micrographs showing the surface morphology of the oxidized NiCrAlY coating after two cycles at 1200 °C.

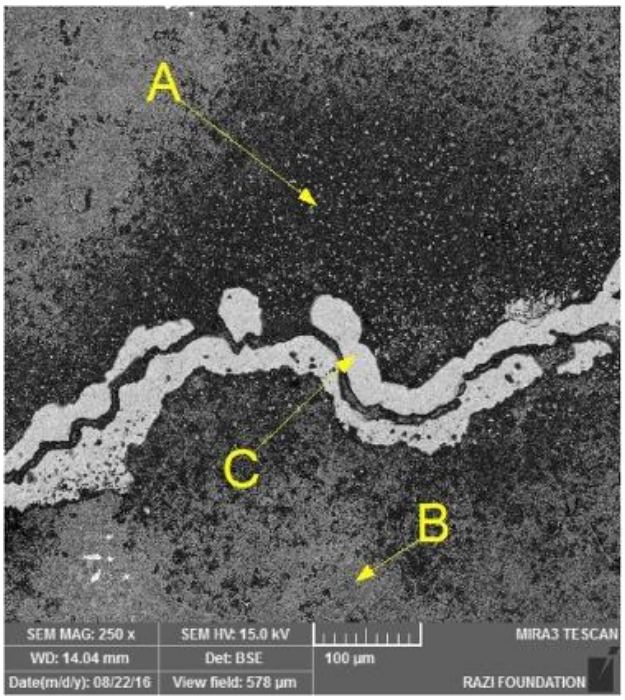

Fig. 9. High-magnification backscatter electron SEM micrograph of the selected region shown in Fig. 8.

Table 2. Chemical composition of the typical phases in Fig. 9.

Zone	Composition (at.%)					Possible phase
Empty Cell	**Ni**	**Cr**	**Al**	**Y**	**O**	Empty Cell
A	0.52	1.05	31.28	1.17	65.99	Al_2O_3
B	0.57	1.39	24.65	8.65	64.74	$Al_5Y_3O_{12}$
C	55.32	21.72	11.20	0.78	10.98	NiCrAlY

Similar phases were characterized on the top surface of the oxidized test piece after ten cycles (Fig. 10). Additionally, cracks, and spallation could be seen on the surface of the oxide scale. The temperature was sufficiently high to form these defects during oxidation. The gray scale ($Al_5Y_3O_{12}$) seemed to be inhomogeneous while black phases (α-Al_2O_3) were more visible. The white phases (bare coating) were randomly present on the top surface, showing local spallation of alumina scale.

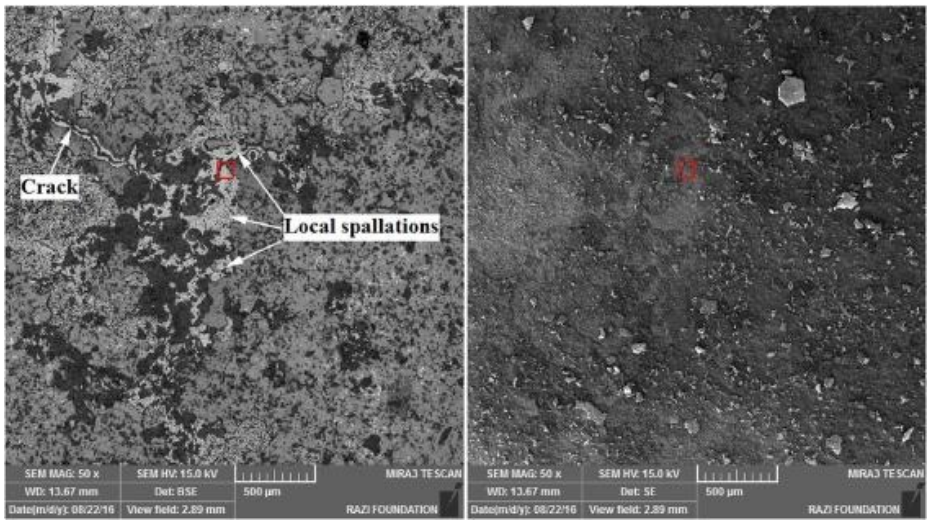

Fig. 10. Low-magnification backscatter and secondary electron SEM micrographs showing the surface morphology of the oxidized NiCrAlY coating after ten cycles at 1200 °C.

The high magnification SEM micrograph of the surface morphology of the oxidized coating after ten cycles (Fig. 11) shows that the black phases were developing around the white phases. It seems that during oxidation the white phases were being consumed to form the black phases, and thus these white areas are the bare coating that was being re-oxidized after local spallation of the alumina scale. Interestingly, voids were more evident on the bare coating after local spallation. In fact, these voids were formed at scale/coating interface, and thus they can be seen on the bare coating after local spallation of the scale. Moreover, the gray scale appeared not to be adherent and it experienced severe spallation after ten cycles. It seems that the outer thin non-protective $Al_5Y_3O_{12}$ scale started to spall completely, whereas alumina scale only experienced local spallation at some spots and rapid re-growth.

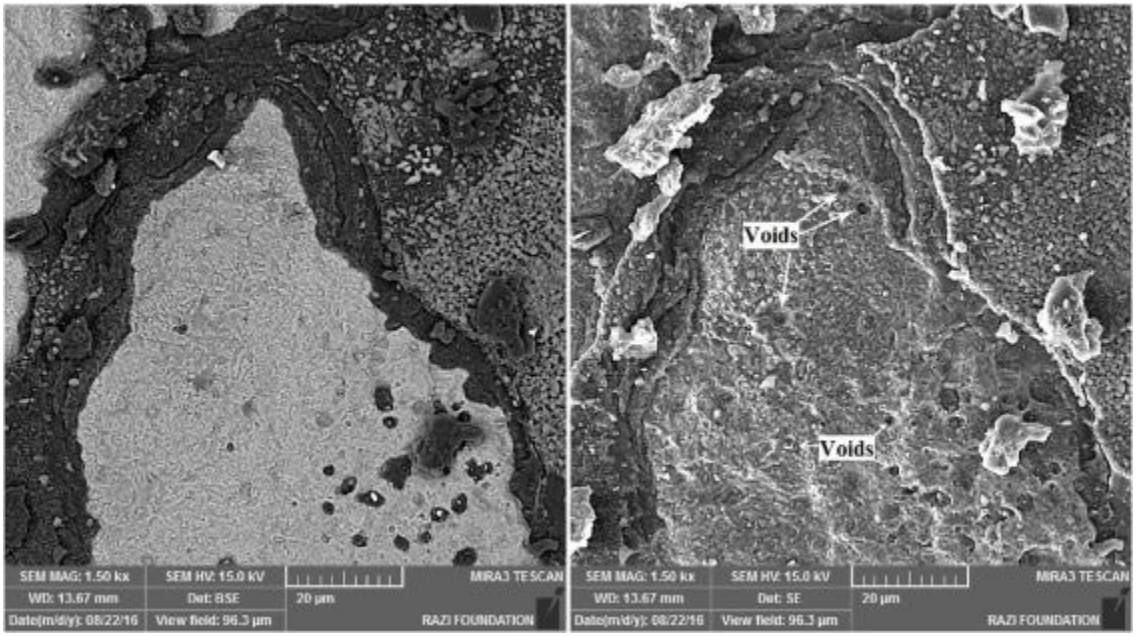

Fig. 11. High-magnification backscatter and secondary electron SEM micrographs of the selected region shown in Fig. 10.

4. Discussion

4.1. Microstructure evolution

The pseudo-binary phase diagram of the ternary Ni-Cr-Al system has been calculated and drawn by Thermo-Calc Software TCNI8 Ni-based superalloys database version 8 [34]. Fig. 12 presents the calculated pseudo-binary phase diagram. According to this diagram, NiCrAlY alloys may contain three major phases: first, γ-Ni phase, an FCC solid solution that can solve Cr in itself; second, γ´-Ni_3Al phase, an ordered FCC ($L1_2$) intermetallic phase; and third, β-NiAl phase, an ordered BCC structure (B2) intermetallic phase. Other solid state precipitated phase, like α-Cr, is not taken into account because it does not affect solidification [21].

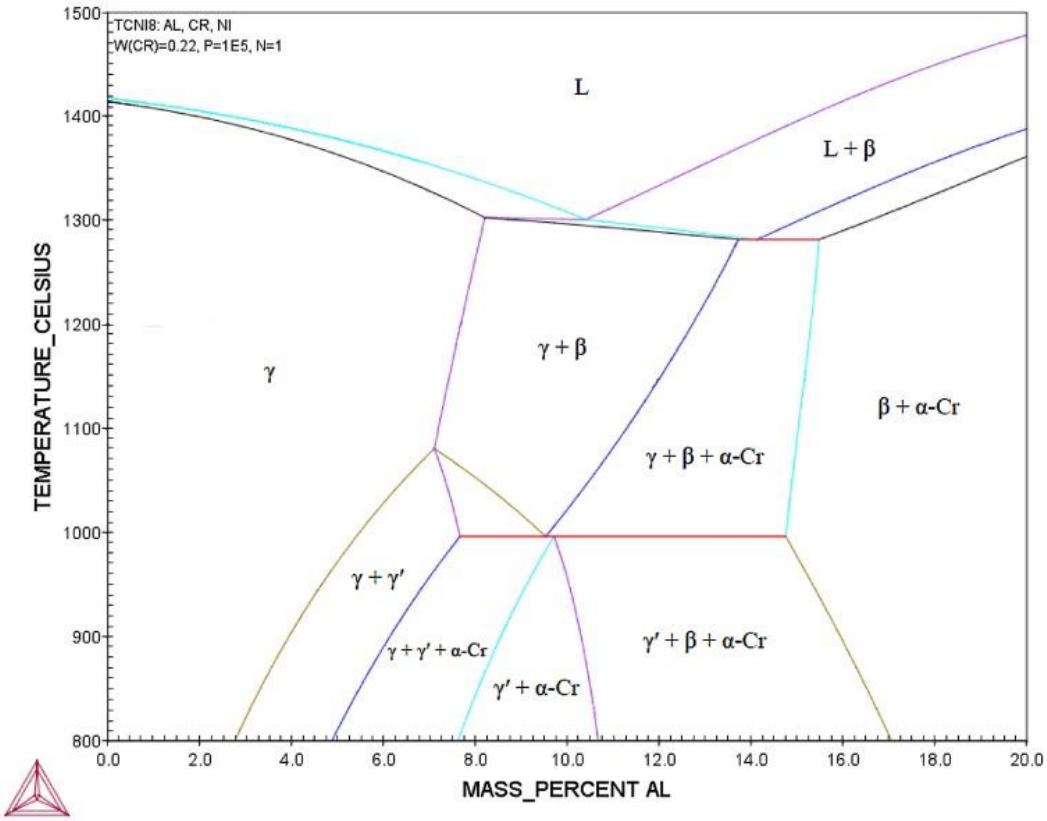

Fig. 12. Pseudo-binary phase diagram of the Ni-Cr-Al system calculated by Thermo-Calc Software TCNI8 Ni-based superalloys database version 8 (Data

taken from reference [34]). The phase boundaries resulting from the variation of Al and Ni contents are calculated, while the Cr content is kept constant at 22 wt.%. The Al content varies between 0 and 20 wt.% whereas Ni is added to give 100 wt.%. Here, γ-Ni is an FCC solid solution that can solve Cr in itself; γ´-Ni_3Al is an ordered FCC ($L1_2$) intermetallic phase; β-NiAl is an ordered BCC structure (B2) intermetallic phase; and α-Cr is a BCC chromium enriched solid state phase.

The pseudo-binary phase diagram is generally calculated in equilibrium conditions, but high cooling rate induced by LAM process can be considered as non- or semi-equilibrium conditions and shift solidus lines in the phase diagram. Despite this, the phase diagram can be useful for predicting the phase formation in the system. When the γ/β NiCrAlY alloy is hypo-eutectic (8–10.5 wt.% Al), the primary solidification phase is γ dendrites. β phase is formed in the interdendritic regions by the residual eutectic reaction at the end of solidification and solid state precipitation of γ´ phase cannot occur. Nucleation is avoided and the oriented columnar γ dendrites are observed in the lower part of the coating. The transition to the un-oriented structure can take place in the upper part of the coating as a result of the stray grain formation in the constitutional undercooling region. The microstructural evolution is related to the extent of constitutional undercooling in the liquid ahead of the solidification front. At the bottom of the molten pool without significant liquid undercooling, the energy barrier of solidification is zero and consequently oriented columnar growth is kinetically preferred in comparison with homogeneous or heterogeneous nucleation. At distant points from the bottom of the molten pool, a constitutional undercooling is generated. As a result, the liquid undercooling may be greater than the critical undercooling for

heterogeneous nucleation, causing the formation of stray grains with random crystallographic orientations [21], [22].

4.2. High-temperature oxidation behavior

In the case of the laser-aided additively manufactured NiCrAlY coatings, the oxidation behavior can be described by the consumption level of Al reservoir for scale formation, and the role of Y as a reactive element in alumina scale. For alumina-forming coatings, the oxidation lifetime will be defined in terms of the consumption level of Al reservoir that is related to the initial Al content, alumina growth rate, critical Al content, rate of scale spallation, and specimen thickness. On the other hand, Y as a reactive element has some positive effects such as reduction in the alumina scale growth rate, suppression of void formation at the scale/coating interface, and improved scale adherence.

It has been reported that reactive elements contribute to reducing the scale growth rate by grain boundary segregation of ions of reactive elements, resulting in changing the transport mechanism. As for scale adherence, key components for justifying improved scale adherence are impurities and reactive elements segregation at the metal/scale interface, which affect interface strength and the formation of interfacial defects. In addition to interfacial segregation, reactive elements can reduce void formation at the metal/scale interface. They affect surface energy and consequently inhibit interfacial void growth. As a result, the doped scale by reactive elements will consume the Al reservoir more slowly and have a prolonged lifetime [11].

In the latest report by Jedliński et al. [35] on the oxidation behavior of Y-implanted β-NiAl alloy at 1200 °C, the alumina scale growth mechanism was explained in three consecutive stages: (i) outward growth mechanism; (ii) mixed outward-inward growth mechanism, with predominant outward growth;

(iii) mixed inward-outward growth mechanism, with predominant inward growth.

The outward growth mechanism (i) occurs in the scale composed of transient Al_2O_3 phases, predominantly θ-Al_2O_3. Yttrium eliminates the inward diffusion of oxygen during the early stage of the oxidation [35]. In fact, the scale starts to grow because of the outward diffusion of aluminum. The presence of voids at the scale/coating interface, as it can be seen in Fig. 11, is an evidence for the outward diffusion of Al atoms across the scale/coating interface as these interfacial voids are characteristics of systems with mobile cations. As for the outward diffusion of Al, the majority of previous studies on the oxidation behavior of both aluminide-type diffusion and MCrAlY overlay coatings containing β-NiAl phase reported that the decomposition of β-NiAl into γ´-Ni_3Al phase contribute to the outward diffusion of the Al that brings about aluminum depletion towards the oxide scale [36]. Tolpygo et al. [36] reported that the precipitated phase from β-NiAl is γ-Ni(Cr) solid solution instead of γ´-Ni_3Al in the case of γ/β MCrAlY coatings with high chromium content. In addition, γ´-Ni_3Al phase is not stable at 1200 °C, regardless of the Al content, as it is clearly shown in Fig. 12. If γ´-Ni_3Al phase could form at temperatures below 1100 °C, it would decompose into γ-Ni(Cr) at temperatures above 1100 °C. That is a possible explanation that why γ and β phases were identified after oxidation tests, whereas γ´-Ni_3Al phase was not detected. By the oxidation time increasing, the relative intensity of β-NiAl became weaker, and the relative intensity of γ-Ni phase became stronger because of the subscale consumption of β and its transformation to γ, as it was proved by XRD results (See Fig. 5).

On the other hand, since the test pieces were inside of the furnace during heating from 25 °C to 1200 °C, the formation of transient alumina phases can be quite probable upon exposure to temperatures below 1100 °C. By

increasing the temperature to above 1100 °C and prolonged oxidation exposures, the transformation from θ-Al_2O_3 to α-Al_2O_3 takes place. This transformation during oxidation is accompanied by a significant volumetric change (as high as 12%), which can lead to crack formation [37]. This is a possible reason for the presence of cracks in the alumina scale, as can be seen in Fig. 8, Fig. 10. These cracks offer fast diffusion paths for the inward penetration of oxygen toward the scale/coating interface and alumina oxide starts to re-oxidize and fill the cracks.

The contribution of the inward growth mechanism of α-Al_2O_3 by the penetration of oxygen toward the scale/coating interface via cracks as well as the contribution of the initial stages of oxide formation in cracks are responsible for the outward-inward growth mechanism (ii). The inward-outward growth mechanism (iii) appears in scales that consist of α-Al_2O_3 by the contribution of the inward transport of oxygen through the α-Al_2O_3 grain boundaries and outward migration of Al at the later stages of filling the cracks with oxide, as well as the outward dislocation-climbing mechanism in α-Al_2O_3 [35]. Meanwhile, the outward transport of Y can also take place upon the oxidation. Y primarily exists as Ni-Y intermetallics. These intermetallics move from the coating to the higher oxygen potential at the reaction front. As the inward transport of oxygen takes place, the intermetallics can convert to $Al_5Y_3O_{12}$ at the scale/coating interface when they are entering the alumina scale. The Ni content of the intermetallics diffuses back into the coating matrix [38]. This incorporation of Y as $Al_5Y_3O_{12}$ in the scale leads to a depletion of Y from the underlying coating. As diffusion to the higher oxygen potential continues, the $Al_5Y_3O_{12}$ phase can move through alumina scale and eventually concentrate on the surface of alumina scale to form the outer thin non-protective $Al_5Y_3O_{12}$ oxide. This thin non-protective scale is not adherent enough to

withstand thermal shocks and its spallation is expected as it can be seen in Fig. 8, Fig. 10. The decrease in the intensity of $Al_5Y_3O_{12}$ phase in XRD patterns could clearly show that this phase was being spalled (See Fig. 5). In systems that cations are mobile, stresses arise in the scale because of the outward diffusion of the metal atoms across the scale/coating interface. Large voids will form at the scale/coating interface, spalling the scale from the underlying coating. The reactive element Y can act as vacancy sinks to suppress void formation at the scale/coating interface [39]. In the present study, the presence of few small voids at the scale/coating interface can prove the positive effect of Y as a reactive element to suppress the void formation. On the other hand, the coefficient of thermal expansion (CTE) mismatch between the alumina scale and the underlying coating dominates scale adhesion owing to large stresses upon cooling process. The scale spallation occurs when the strain energy in the scale (originated from the CTE mismatch) is more than the strength of the interface [11]. It has been reported that the large $Al_5Y_3O_{12}$ particles (as they are evident in Fig. 6) can concentrate the stresses during cooling after long exposure time [40]. As a result of the concentrated stresses, cracks initiate next to the $Al_5Y_3O_{12}$ particles and propagate through the alumina scale. As discontinuous and cyclic oxidation with repeated heating and cooling can increase the crack growth and linking processes, the alumina scale can locally spall off the underlying coating at areas in the vicinity of large $Al_5Y_3O_{12}$ particles. However, the Al content is still high enough for rapid re-oxidation of Al and fill the locally spalled areas. Subsequently, the continuity of the formation of Al_2O_3 and $Al_5Y_3O_{12}$ depletes a large amount of Al and Y content owing to the selective oxidation. An aluminum- and yttrium-depleted zone develops and tends to increase in size with more oxidation time. After ten cycles of oxidation, it seems the Y content of the underlying NiCrAlY coating is about to end due to repetitive formation

and spallation of $Al_5Y_3O_{12}$ oxide. However, the Al content of the NiCrAlY coating is large enough to continue forming alumina scale. The outward diffusion of Ni and Cr cannot occur due to the higher diffusion coefficient of Al compared to Ni and Cr and these elements are only present below the scale/coating interface (as it can be seen in Fig. 6, Fig. 7). As the aluminum-depleted zone develops and the Al content is not enough to form alumina scale, diffusion of Ni and Cr will take place. Providing the Al content drops down below the critical value for alumina formation, Cr and Ni will be oxidized. In the present study, no NiO, Cr_2O_3 and $Ni(Cr,Al)_2O_4$ spinel was detected in the scale after ten cycles of the oxidation at 1200 °C (as it was proven by XRD results in Fig. 5). This shows that there is still enough Al reservoir for alumina formation and re-growth after local spallation.

Despite all positive effects of reactive element Y on the alumina scale, there are additional considerations in the case of MCrAlY-type overlay coatings containing reactive elements. These considerations are oxygen content, thickness, and roughness of the coating [11]. The first consideration is the effect of coating oxygen content. The oxygen content leads to significant changes in the oxidation behavior, affecting the lifetime of compositionally the same coating. In the manufacturing of a coating, a considerable variation in the oxygen content may occur depending on the manufacturing method (LPPS, HVOF, APS, or LAM) and processing parameters. During manufacturing of coatings, some or all reactive elements can be tied up as relatively immobile oxides in the coating and suppress the positive effect of reactive elements on scale adhesion [11]. The second consideration is the effect of coating thickness. It has been reported that the optimum level of reactive elements is affected by the coating thickness. Thus, thick coatings are over-doped because the total reservoir of reactive elements is more than

what is needed. In the case of thick MCrAlY coatings, an extensive precipitation of Y-oxides and Y-rich oxide pegs in the scale has been observed [11]. The third consideration is the effect of coating roughness. The variation of roughness leads to inhomogeneous incorporation of reactive elements into the oxide scale. A thin oxide scale, relatively pure alumina, is formed on the hills of rough MCrAlY coatings, whereas a scale containing higher amounts of Y-rich oxide pegs is formed in the valleys. This implies that on rough MCrAlY coatings, more inhomogeneous alumina scales can be formed compared to smooth coatings with the same composition.

Having considered these additional considerations, comparing the results of the present study with another study on the oxidation behavior of thermally sprayed NiCrAlY coatings at 1200 °C can shed light on the understanding of superior oxidation resistance of laser-aided additively manufactured NiCrAlY coating. Strawbridge et al. [29] investigated the oxidation behavior of APS NiCrAlY coatings at 1200 °C and reported the formation of a protective alumina scale during the early stages of oxidation. However, an increased rate of weight gain following with enhanced growth of Ni-rich oxides and breakaway oxidation occurred after 30 h exposure. The average scale thickness after 100 h exposure was about 50 μm and large individual voids (10 μm in size) in the spallation zone were the critical defects for failure. Serghini et al. [30] also investigated the oxidation behavior of HVOF NiCrAlY coatings at 1200 °C. They reported that the quality of HVOF coatings is most likely responsible for the oxidation behavior, due to the fact that little porosity may dramatically affect the oxidation rate.

Reviewing previous studies on the oxidation behavior of thermally sprayed NiCrAlY coatings clearly shows that the initial quality of NiCrAlY coatings as

well as the microstructure and chemical composition with regard to the manufacturing process and processing parameters, are the main determinant of their oxidation life and can affect positive effects of reactive element Y. In comparison to thermally sprayed NiCrAlY coatings, reactive element Y in the laser-aided additively manufactured NiCrAlY coating effectively contributed to the reduction of the Al reservoir consumption rate, resulting in a prolonged lifetime. In addition, it reduced the scale growth rate so that the average scale thickness after ten cycles was about 8 μm. Large interfacial voids were not observed in the oxidized coating manufactured through LAM process. Although some Y-rich oxide pegs probably formed because of the high thickness of the coating and could lead to local spallation in Y-rich areas, the Al reservoir was enough for rapid re-growth of alumina in locally spalled areas and postpone the formation of Ni- or Cr-rich oxides and breakaway oxidation. Thermally sprayed coatings intrinsically have inhomogeneous microstructure as well as porosities and rough surfaces, which can suppress the positive effects of reactive element Y and allow oxygen to diffuse through the coatings and consequently decrease the oxidation lifetime. However, dense coatings manufactured through LAM process with homogeneous microstructures and smooth surfaces can trigger the positive effects of reactive element Y and consequently increase the oxidation lifetime. As the Y element diffuses from the coating to the higher oxygen potential at the reaction front, dense, fine, and dendritic structures manufactured through LAM process can facilitate Y-diffusion towards the scale/coating interface compared to porous and lamellar structures manufactured by thermal spraying processes. On the other hand, the transformation of β to γ phase during oxidation is associated with a volume reduction which is the main reason of rumpling and cavity formation during cyclic and isothermal oxidation. It has been reported that reactive elements in alumina scale can improve its creep strength and consequently

inhibit rumpling which is another positive effect of reactive elements by forming a smooth alumina scale [11].

The effect of Y as a reactive element during oxidation of laser-aided additively manufactured NiCrAlY coatings have not been discussed yet. Thus, further studies are needed to get a better understanding of the degradation of the coatings at 1200 °C and connect these new observations to the current understanding of various aspects of the effects of reactive elements.

5. Conclusions

The LAM-based approach was successfully employed to additively manufacture NiCrAlY coatings on IN738 superalloy for high-temperature oxidation protection and the following conclusions can be drawn:

1. The lower part of the coating was composed of oriented columnar γ dendrites with interdendritic β phase. However, oriented γ/β structure transitioned to un-oriented γ/β structure in the middle of the coating and stray grains were largely observed in the upper part of the coating.
2. The NiCrAlY coating showed a steep rise in weight gain at early stages of oxidation.
3. The oxide scale formed on the coating after two cycles was mainly composed of α-Al_2O_3 scale while $Al_5Y_3O_{12}$ islands and pegs were extensively dispersed in the alumina scale.
4. After three to ten cycles, the NiCrAlY coating showed a trend of slower weight gain and the average oxidation kinetics declined.

5. The oxide scale formed on the coating after ten cycles was composed of α-Al_2O_3 scale with a few $Al_5Y_3O_{12}$ islands and pegs.
6. The main reason why the NiCrAlY coating manufactured through LAM process could operate beyond 1100 °C was mainly ascribed to the microstructure and chemical composition of the coating, which can stimulate the positive effects of yttrium as a reactive element on the alumina scale adhesion, growth, and microstructure.

Acknowledgments

The authors would like to thank Dr. G.R. Gordani for providing the oxidation testing facilities.

References

[1] Y. Ding, R. Kovacevic

Feasibility study on 3-D printing of metallic structural materials with robotized laser-based metal additive manufacturing
JOM, 68 (2016), pp. 1774-1779, 10.1007/s11837-016-1929-7

[2] M. Seifi, A. Salem, J. Beuth, O. Harrysson, J.J. Lewandowski

Overview of materials qualification needs for metal additive manufacturing
JOM, 68 (2016), pp. 747-764, 10.1007/s11837-015-1810-0

[3] N.B. Dahotre, H.D. Vora, B. Boesl

Additive manufacturing via surface engineering
JOM, 68 (2016), pp. 1759-1761, 10.1007/s11837-016-1955-5

[4] Z. Zhang, P. Farahmand, R. Kovacevic

Laser cladding of 420 stainless steel with molybdenum on mild steel A36 by a high power direct diode laser
Mater. Des., 109 (2016), pp. 686-699, 10.1016/j.matdes.2016.07.114114

[5] M. Ansari, H. Ramezani, S. Yari, R. Soltani

Pulsed Nd:YAG laser surface alloying of AZ31 magnesium with nickel for improved wear and corrosion resistance

J. Laser Appl., 28 (2016), p. 012013, 10.2351/1.4937429

[6] M. Ansari, R. Soltani, M. Heydarzadeh Sohi, Z. Valefi

Microstructural and hardness study of pulsed Nd:YAG laser surface alloyed aluminum with iron

Metall. Mater. Trans. A, 47 (2016), pp. 1698-1704, 10.1007/s11661-015-3320-7

[7] M. Ansari, M. Heydarzadeh Sohi, R. Soltani, M.J. Torkamany

Effect of pulsed Nd:YAG laser re-melting on chromium surface alloyed AA6061-T6 aluminum

Int. J. Adv. Manuf. Technol., 83 (2016), pp. 285-291, 10.1007/s00170-015-7516-1

[8] M.J. Pomeroy

Coatings for gas turbine materials and long term stability issues

Mater. Des., 26 (2005), pp. 223-231, 10.1016/j.matdes.2004.02.005

[9] W.R. Chen, X. Wu, B.R. Marple, P.C. Patnaik

Oxidation and crack nucleation/growth in an air-plasma-sprayed thermal barrier coating with NiCrAlY bond coat

Surf. Coat. Technol., 197 (2005), pp. 109-115, 10.1016/j.surfcoat.2004.06.027

[10] E.A.G. Shillington, D.R. Clarke

Spalling failure of a thermal barrier coating associated with aluminum depletion in the bond-coat

Acta Mater., 47 (1999), pp. 1297-1305, 10.1016/S1359-6454(98)00407-8

[11] D. Naumenko, B.A. Pint, W.J. Quadakkers

Current thoughts on reactive element effects in alumina-forming systems: in memory of John Stringer

Oxid. Met., 86 (2016), pp. 1-43, 10.1007/s11085-016-9625-0

[12] M.H. Guo, Q.M. Wang, J. Gong, C. Sun, R.F. Huang, L.S. Wen

Oxidation and hot corrosion behavior of gradient NiCoCrAlYSiB coatings deposited by a combination of arc ion plating and magnetron sputtering techniques
Corros. Sci., 48 (2006), pp. 2750-2764, 10.1016/j.corsci.2005.09.014

[13] F.H. Yuan, Z.X. Chen, Z.W. Huang, Z.G. Wang, S.J. Zhu

Oxidation behavior of thermal barrier coatings with HVOF and detonation-sprayed NiCrAlY bondcoats
Corros. Sci., 50 (2008), pp. 1608-1617, 10.1016/j.corsci.2008.02.002

[14] C.Z. Xu, S.M. Jiang, Z.B. Bao, J. Gong, C. Sun

Isothermal oxidation behaviour of a gradient NiCoCrAlSiY coating deposited by arc ion plating on a Ni-based single crystal superalloy
Corros. Sci., 51 (2009), pp. 1467-1474, 10.1016/j.corsci.2009.03.036

[15] S.M. Jiang, H.Q. Li, J. Ma, C.Z. Xu, J. Gong, C. Sun

High temperature corrosion behaviour of a gradient NiCoCrAlYSi coating II: oxidation and hot corrosion
Corros. Sci., 52 (2010), pp. 2316-2322, 10.1016/j.corsci.2010.03.032

[16] M. Chen, S. Zhu, F. Wang

High temperature oxidation of NiCrAlY, nanocrystalline and enamel-metal nano-composite coatings under thermal shock
Corros. Sci., 100 (2015), pp. 556-565, 10.1016/j.corsci.2015.08.033

[17] M. Shen, P. Zhao, Y. Gu, S. Zhu, F. Wang

High vacuum arc ion plating NiCrAlY coatings: microstructure and oxidation behavior
Corros. Sci., 94 (2015), pp. 294-304, 10.1016/j.corsci.2015.02.032

[18] J. Wang, M. Chen, L. Yang, S. Zhu, F. Wang

Comparative study of oxidation and interdiffusion behavior of AIP NiCrAlY and sputtered nanocrystalline coatings on a nickel-based single-crystal superalloy
Corros. Sci., 98 (2015), pp. 530-540, 10.1016/j.corsci.2015.05.062

[19] Y.Z. Liu, X.B. Hu, S.J. Zheng, Y.L. Zhu, H. Wei, X.L. Ma

Microstructural evolution of the interface between NiCrAlY coating and superalloy during isothermal oxidation
Mater. Des., 80 (2015), pp. 63-69, 10.1016/j.matdes.2015.05.014

[20] H. Choi, B. Yoon, H. Kim, C. Lee

Isothermal oxidation of air plasma spray NiCrAlY bond coatings
Surf. Coat. Technol., 150 (2002), pp. 297-308,

[21] C. Bezençon, A. Schnell, W. Kurz

Epitaxial deposition of MCrAlY coatings on a Ni-base superalloy by laser cladding
Scr. Mater., 49 (2003), pp. 705-709, 10.1016/S1359-6462(03)00369-5

[22] R. Vilar, A. Almeida

Repair and manufacturing of single crystal Ni-based superalloys components by laser powder deposition—a review
J. Laser Appl., 27 (2015), p. S17004

http://dx.doi.org/10.2351/1.4862697

[23] K. Partes, C. Giolli, F. Borgioli, U. Bardi, T. Seefeld, F. Vollertsen

High temperature behaviour of NiCrAlY coatings made by laser cladding
Surf. Coat. Technol., 202 (2008), pp. 2208-2213, 10.1016/j.surfcoat.2007.09.010

[24] H. Wang, D. Zuo, J. Yan, M. Huang, X. Li

Effects of nanometer Al2O3 particles on oxidation behaviors of laser cladding low Al NiCoCrAlY coatings
Oxid. Met., 74 (2010), pp. 49-60, 10.1007/s11085-010-9197-3

[25] M.J. Tobar, J.M. Amado, A. Yáñez, J.C. Pereira, V. Amigó

Laser cladding of MCrAlY coatings on stainless steel

Phys. Procedia, 56 (2014), pp. 276-283, 10.1016/j.phpro.2014.08.172

[26] J.C. Pereira, J.C. Zambrano, M.J. Tobar, A. Yañez, V. Amigó

High temperature oxidation behavior of laser cladding MCrAlY coatings on austenitic stainless steel

Surf. Coat. Technol., 270 (2015), pp. 243-248, 10.1016/j.surfcoat.2015.02.050

[27] H. Iwamoto, T. Sumikawa, K. Nishida, T. Asano, M. Nishida, T. Araki

High temperature oxidation behavior of laser clad NiCrAlY layer

Mater. Sci. Eng. A, 241 (1998), pp. 251-258, 10.1016/S0921-5093(97)00499-1

[28] S. Zhou, Z. Xiong, J. Lei, X. Dai, T. Zhang, C. Wang

Influence of milling time on the microstructure evolution and oxidation behavior of NiCrAlY coatings by laser induction hybrid cladding

Corros. Sci., 103 (2015), pp. 105-116, 10.1016/j.corsci.2015.11.011

[29] A. Strawbridge, H.E. Evans, C.B. Ponton

Spallation of oxide scales from NiCrAlY overlay coatings

Mater. Sci. Forum, 251–254 (1997), pp. 365-372, 10.4028/www.scientific.net/MSF.251-254.365

[30] S. Serghini, S. Dallaire

Cyclic and isothermal oxidationat 1200 °C of HVOF NiCrAlY sprayed coatings

C.C. Berndt (Ed.), Thermal Spray: Surface Engineering via Applied Research: Proceedings of the 1st International Thermal Spray Conference, ASM International Montreal, Canada (2000), pp. 1005-1009

[31] F. Brossa, D. D'Angelo, E. Gandini

Structure and composition of MCrAlY coatings modified by Al additions

J. Phys. IV France, 03 (1993), pp. 559-568

http://dx.doi.org/10.1051/jp4:1993959

[32] M. Ansari, R. Shoja Razavi, M. Barekat

An empirical-statistical model for coaxial laser cladding of NiCrAlY powder on Inconel 738 superalloy

Opt. Laser Technol., 86 (2016), pp. 136-144, 10.1016/j.optlastec.2016.06.014

[33] S.R.J. Saunders, J.R. Nicholls

Chapter 14 - Oxidation, hot corrosion and protection of metallic materials
R.W. Cahn, P. Haasen (Eds.), Physical Metallurgy (Fourth, Revised and Enhanced Edition), Oxford, North-Holland (1996), pp. 1352-1354

http://dx.doi.org/10.1016/B978-044489875-3/50019-3

[34] **Thermo-Calc Software TCNI8 Ni-based Superalloys Database Version 8**

(2016)

(Accessed 19 January 2016)

[35] J. Jedliński, R. Gołdyn, J.-L. Grosseau-Poussard, G. Bonnet, K. Kowalski, A. Bernasik, *et al.*

Oxide phases and residual stresses in scales formed at early stages of oxidation of β-NiAl at 1473 K and the effect of implanted yttrium

Mater. Corros., 68 (2017), pp. 235-248

http://dx.doi.org/10.1002/maco.201508774

[36] V.K. Tolpygo, D.R. Clarke

Surface rumpling of a (Ni, Pt)Al bond coat induced by cyclic oxidation
Acta Mater., 48 (2000), pp. 3283-3293, 10.1016/S1359-6454(00)00156-7

[37] B.A. Pint, M. Treska, L.W. Hobbs

The effect of various oxide dispersions on the phase composition and morphology of Al2O3 scales grown on β-NiAl
Oxid. Met., 47 (1997), pp. 1-20, 10.1007/BF01682369

[38] T.A. Ramanarayanan, M. Raghavan, R. Petkovic-Luton

Metallic yttrium additions to high temperature alloys: influence on Al2O3 scale properties
Oxid. Met., 22 (1984), pp. 83-100, 10.1007/BF00656898

[39] N. Birks, G.H. Meier, F.S. Pettit

Introduction to the High-Temperature Oxidation of Metals
(2nd edition), Cambridge University Press, Cambridge (2006), 10.2277/0521480426

[40] J.D. Kuenzly, D.L. Douglass

The oxidation mechanism of Ni3Al containing yttrium

Oxid. Met., 8 (1974), pp. 139-178, 10.1007/BF00612170